


Dynamic Modelling and Experimental Analysis of an Offshore Crane Payload Positioning System with a Parallel Cable-Driven Method

Zhaopeng Ren¹

Zhe Huang¹ 

Tingqi Zhao¹

Shenghai Wang*^{1,2}

Yuqing Sun^{1,2}

Haiquan Chen^{1,2}

Nan Fang¹ 

¹ Marine Engineering College, Dalian Maritime University, Dalian, China

² National Center for International Research of Subsea Engineering Technology and Equipment, Dalian Maritime University, Dalian, China

* Corresponding author: shenghai_wang@dlnu.edu.cn (Shenghai Wang)

ABSTRACT

The violent swinging motion of a payload imposes significant safety problems for the operation of offshore ship-mounted cranes (offshore cranes). We therefore propose a stable experimental hoisting platform for an offshore crane payload positioning system with a parallel cable-driven method (PP-PCDM), and an adaptive cable-drive anti-swing tension (ACAT) control method based on the PP-PCDM is developed to resolve the problem of swinging of the payload by limiting its spatial position. The PP-PCDM enables synchronous tracking of the movement of the payload when the crane is working. When the payload deviates from a stable state due to an external disturbance, the anti-swing cables are immediately retracted or released based on the feedback signal. The spatial position of the payload is then limited by adjusting the length and tension of the parallel cables until the payload appears stationary from the perspective of the ship's deck. Operational safety and efficiency is substantially improved, and the proposed PP-PCDM structure and ACAT control method can be applied to a variety of different types of cranes. The results of simulations and physical experiments show that the anti-swing effect exceeds 89.86%. The PP-PCDM enables excellent performance of synchronous tracking and hoisting assistance, and ensures that the rated lifting weight of the offshore crane is not affected.

Keywords: offshore cranes; payload positioning system; cable drive; dynamic analysis

INTRODUCTION

With the rapid development of high-quality of ocean engineering equipment technology, it is well-known that the sizes, weights and importance of lifting payloads are becoming larger, and the price is also becoming higher. The safety of the hoisting process is particularly important when offshore cranes are working in heavy ocean conditions in a marine environment, and especially when this involves helicopters, wind power equipment or warship supplies. As offshore cranes

suffer from motion excitation in six degrees of freedom from persistent or intermittent unexpected disturbances induced by ocean waves or wind, the stability of the lifting operation is vitally important, and can have a decisive effect on the progress of a project. Any type of accident can cause extensive property damage, and can even endanger the lives of workers on the deck and delay engineering processes [1].

Studies of the orientation of offshore cranes have mainly focused on two aspects: installing a variety of sensors, or using different mechanical structures. In the former approach, the

mechanical structure of the offshore crane is not changed, but the swinging motion of the payload is controlled by feedback signals. In the latter, a mechanical structure is added to the crane, and the swinging motion of the payload is controlled by limiting the spatial position of the payload. As increasing numbers of experts and scholars are entering the field of research on offshore cranes, innovative mechanical structures and control methods are emerging. This not only means that the maturity of offshore crane technology has increased, but that the development of advanced technology has greatly promoted progress in this area. A double-pendulum dynamic model of an offshore crane was built in which the drive forces were functions of Fourier series based on the bridge cranes. A verification of the simulation was presented in which the open-loop control method increased the instability of the system [2]. A model prediction method was proposed for an anti-swing control study of a jib-type Liebherr harbour crane. A traditional track computing method was optimised to achieve a good tracking effect on a knuckle boom crane. A nonlinear PID controller was also studied to address the issue of low power consumption of the crane [3]-[5]. Researchers have also analysed the dynamic characteristics of the rope, and have studied the problem of collisions in the payload hoisting operation, with improvements in the accuracy of dynamic modelling [6],[7]. An adaptive and automatic positioning control method based on synchronous learning was proposed that enabled a fast response and trajectory tracking for the system [8],[9]. Although existing control methods can restrain the swinging motion of the payload, the dynamic model of the ocean waves and ship is relatively simple, and the analysis of the swing space of payload has been neglected. Another obvious issue with existing research is the absence of experimental verification, as the device has not been widely used in practice engineering application.

In view of the flexible characteristics of the cable, numerous experts and scholars around the world have proposed solutions for the under-actuation problem, which arises in particular when an offshore crane is working under heavy ocean conditions. An event-triggered control approach and a nonlinear controller is used for the crane, and the convergence time and mechanical chattering can be reduced. The payload swing signals and the rope positioning error are used as feedback, and this approach achieves better overall control performance, which also guarantees the positioning accuracy of the trolley [10]-[13]. The problem of under-actuation and anti-swing technology for the crane has been studied, and some research directions have been put forward for reference [14],[15]. The double pendulum problem and the dynamic relationship between the payload and the offshore crane have also been analysed [16],[17]. A method of motion compensation has been proposed to reduce the influence of vibration frequency on the control effect [18], and an original rigid-flexible coupling anti-swing mechanical arm was developed, which was composed of a parallel rigid anti-swing mechanical arm and flexible anti-swing cables. This mechanical structure was shown to assist with the hoisting operation of the offshore crane and to improve the rigidity

of the system. In terms of payload control methods, several methods such as the PID control algorithm, the tension control algorithm [19], the trajectory tracking method [20] and the learning-based adaptive control method [21] have been proposed for anti-swing control of the payload. The stability and effectiveness of the control strategy is very important for the motion of the crane and the anti-swing control of the payload [22],[23]. The security of the offshore crane hoisting operation and structural strength have also been considered [24]. The flexible characteristics of the cable were addressed by optimising the control method, and the control precision over the payload swaying motion was improved. However, the absence of research on the mechanical limit-position method that combined with rigid mechanical arms and flexible cables. An ACAT control method is therefore proposed for an offshore crane with PP-PCDM. The dynamic tension and length of cables can be adjusted according to the real-time feedback signals representing the payload's swinging motion. The spatial position of the payload is limited by the PP-PCDM, and the anti-swing control precision is dramatically improved.

In order to ensure the safety and efficiency of hoisting with offshore cranes, an original offshore crane with PP-PCDM is designed and an adaptive anti-swing control strategy is developed, based on the feedback signals of the payload, to resolve this difficult problem. A dynamic modelling and simulation analysis of the offshore crane system is carried out to verify the feasibility of the proposed method, and an offshore crane anti-swing experiment platform is independently designed and built to enable further study. Finally, the effectiveness, safety and practicability of the proposed PP-PCDM and ACAT control method is verified through digital simulations and physical experiments. The hoisting process can be accomplished safely and efficiently by offshore cranes with PP-PCDM, even if the ship is working under heavy ocean conditions.

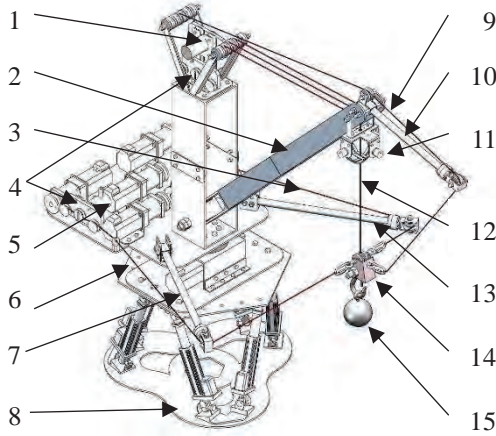
MODELING OF AN OFFSHORE CRANE WITH PP-PCDM

STRUCTURAL DESIGN OF AN OFFSHORE CRANE WITH PP-PCDM

A three-dimensional schematic diagram of the proposed structure for an offshore crane with PP-PCDM is shown in Fig. (1). The crane is composed of a base, a body, a boom, anti-swing cables, anti-swing mechanical arms, a servo motor drive unit, and so on.

Three rigid-flexible coupling mechanical arms are installed on a conventional offshore crane. Mechanical arm I is installed at the lifting point of crane, while mechanical arms II and III are installed on the body of the offshore crane, in a symmetric manner. Anti-swing cables I, II and III are connected to the crane hook via the free end of anti-swing mechanical arms I, II and III, respectively. An angle sensor

is installed at the lifting point of the offshore crane, which can accurately measure and feedback the real-time swing angle of the payload. Tension sensors are installed on the body of the crane, and can accurately measure and feed back the real-time tension of the anti-swing cables and lifting cable. Servo motors are installed at the base of the crane to control the length and speed of the cables. The lifting cable will deviate from the vertical position and form an included angle with the vertical line when the payload is swinging, where the included angle is defined as the swing angle of the payload. In this state, the tension in the lifting cable is less than the gravity of the payload, which reduces the effective lifting weight of the crane. In this way, the cables not only reduce the swinging motion of the payload, but also assist in the hoisting operation to ensure that the rated lifting weight of the crane is not affected.



1. Tension sensors for the lifting cable. 2. Crane boom. 3-6-9. Anti-swing cables II, III and I. 4. Tension sensors for the anti-swing cables. 5. Servo motor drive unit. 8. Ship motion simulation platform. 7-10-13. Anti-swing mechanical arms II, III and I. 11. Angle sensors for the payload. 12. Lifting cable. 14. Crane hook. 15. Payload.

Fig. 1. Diagram of the proposed offshore crane with PP-PCDM

MODELING OF SHIP SWAY UNDER STOCHASTIC EXCITATION FROM OCEAN WAVES

The actual motion of ocean waves is usually stochastic and irregular. To improve the authenticity of the mathematical model of the offshore crane, a stochastic model of ocean waves is built based on the ITTC one-parameter ocean wave spectrum, using the following equation:

$$S(\omega) = \frac{8.1 \cdot 10^{-3} g^2}{\omega^5} \exp\left(-\frac{3.11}{h_{1/3}^2 \omega^4}\right) \quad (1)$$

where the $S(\omega)$ is the energy, ω is the circular frequency, h is the significant wave height of the stochastic ocean waves, and g is the gravitational acceleration.

The spectra of ocean waves at different significant wave heights can be obtained using Equation (1), and the digital simulation curves are shown in Fig. 2.

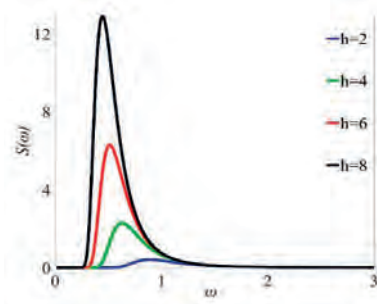


Fig. 2. Spectra for ocean waves of differing heights

We assume that the stochastic ocean waves are created by the superposition of an infinite number of stochastic sine waves with different amplitudes, different frequencies and different phases. The ocean waves therefore conform to the superposition principle. The ocean waves coordinate system $T_1-(o_1-x_1y_1z_1)$ is positioned at the surface of still water, with the origin at the starting point of the ocean waves, and the equation for the stochastic ocean waves is established under the Longuet-Higgins assumption as follows:

$$\xi(t) = \sum_{i=0}^N \bar{\xi}_i \cos(\omega_i t + \varepsilon_i) \quad (2)$$

where the phase angle of a single ocean wave is a stochastic value between 0 and 2π , N is the number of ocean waves, and i represents the i -th ocean wave.

The independent variable is the slope of the surface of an ocean wave when building the dynamic model of the ship's swaying motion. We therefore need to convert the wave amplitude ξ_i into the wave angle ψ_ω to obtain the slope of wave surface of the ocean waves.

$$\psi_\omega = \frac{\omega^2}{g} \xi_i \quad (3)$$

The equation for the slope of the surface of an ocean wave can be obtained by substituting Equations (1) and (2) into Equation (3):

$$\psi_\omega = \frac{\omega^2}{g} \sum_{i=1}^N \cos(\omega t + \varepsilon_i) \sqrt{2 \frac{8.1 \cdot 10^{-3} g^2}{\omega^5} \exp\left(-\frac{3.11}{h^2 \omega^4}\right) \Delta\omega} \quad (4)$$

The parameters for ocean waves under various conditions can be obtained as shown in Table 1.

Tab 1. Parameters of waves under various ocean conditions

| No. | Significant wave height (m) | Wind speed (m/s) | Simulation frequency (rad/s) | Frequency increment (rad/s) |
|-----|-----------------------------|------------------|------------------------------|-----------------------------|
| 1 | <2.5 | <8 | 0.3-3.0 | 0.10 |
| 2 | 2.5-5.0 | 8-12 | 0.25-2.4 | 0.08 |
| 3 | >5.0 | >12 | 0.1-1.7 | 0.06 |

The slope of the surface of a wave under different ocean conditions can be obtained from Equation (4) and Table (1).

We consider rolling of the ship as an example, and establish a dynamic model in the T_2 -($o_2-x_2y_2z_2$) coordinate system under the influence of stochastic ocean waves. The angle φ is the swaying angle of the ship, and clockwise swaying of the ship is taken as positive.

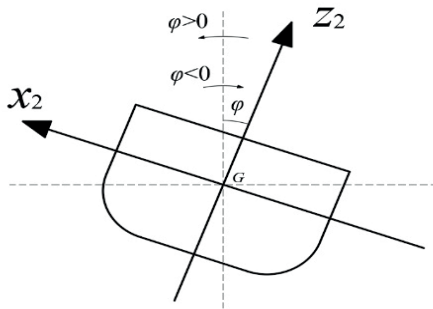


Fig. 3. Diagram showing the ship's swaying motion

The ship is mainly subject to swaying and disturbance moments, including the righting moment, damping moment and inertia moment, but the forces for these moments are different.

The equation used to calculate the ship's swaying moment is as follows:

$$M(\varphi, \dot{\varphi}, \ddot{\varphi}) = Dh\varphi + 2N_{\mu}\dot{\varphi} + (I_x + \Delta I_x)\ddot{\varphi} \quad (5)$$

where the $\dot{\varphi}$ represents the swaying acceleration of the ship, $\ddot{\varphi}$ represents the swaying acceleration of the ship.

To calculate the ocean wave disturbance moment, we use the following equation:

$$M(\psi_m, \dot{\psi}_m, \ddot{\psi}_m) = Dh\psi_m + 2N_{\mu}\dot{\psi}_m + \Delta I_x\ddot{\psi}_m \quad (6)$$

Equation (6) can be simplified based on the dynamic characteristics of the ocean wave as

$$M(\psi_m, \dot{\psi}_m, \ddot{\psi}_m) = Dh\psi_m \quad (7)$$

According to the dynamic balance principle, there is a balancing relationship between the ship swaying moment and the ocean wave disturbance moment. This mathematical relationship can be expressed as follows:

$$M(\phi, \dot{\phi}, \ddot{\phi}) + M(\alpha_m, \dot{\alpha}_m, \ddot{\alpha}_m) = 0 \quad (8)$$

The dynamic differential equation for the ship's swaying motion can be obtained as follows:

$$\ddot{\varphi} = \frac{Dh\omega^2}{(I_x + \Delta I_x)g} \left(\sum_{i=1}^N \cos(\omega t + \varepsilon_i) \sqrt{2 \frac{8.1 \cdot 10^{-3} g^2}{\omega^5} \exp\left(-\frac{3.11}{h^2 \omega^4}\right) \Delta \omega} \right) - \frac{Dh\varphi + 2N_{\mu}\dot{\varphi}}{(I_x + \Delta I_x)} \quad (9)$$

KINEMATIC MODELING OF AN OFFSHORE CRANE WITH PP-PCDM

The diagram of the structure of an offshore crane with PP-PCDM in Fig. (1) can be simplified to the schematic diagram in Fig. (4).

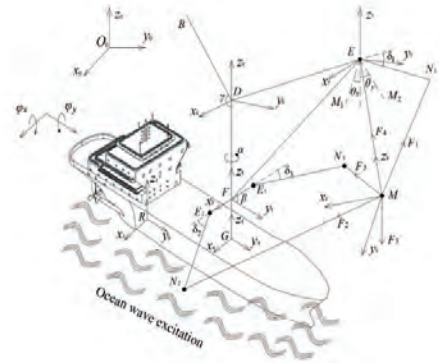


Fig. 4. Schematic diagram of an offshore crane with PP-PCDM

In the figure above, T_0 ($o_0-x_0y_0z_0$) is defined as the global coordinate system; T_3 ($o_3-x_3y_3z_3$) is the inertial coordinate system of the offshore crane; T_4 ($o_4-x_4y_4z_4$) is the ship-based coordinate system; T_5 ($o_5-x_5y_5z_5$) is the coordinate system for operation of the crane; T_6 ($o_6-x_6y_6z_6$) is the coordinate system for the cables; T_7 ($o_7-x_7y_7z_7$) is the coordinate system for the lifting point; and T_8 ($o_8-x_8y_8z_8$) is the stable coordinate system. Point R represents the centre of sway of the ship; point G is the location of the installation of the offshore crane on the ship; point F is the central point for slewing and luffing of the offshore crane operation; point E is the lifting point of the offshore crane; and point M is the mass point of hook and payload. The line FE is the crane boom, with length labelled as L_{FE} ; H is the length of the lifting cable; L_I , L_{II} and L_{III} are the lengths of the anti-swing mechanical arms I, II and III, respectively; and L_1 , L_2 and L_3 are the lengths of the anti-swing cables I, II and III, respectively. δ_1 , δ_2 and δ_3 are the included angles of the anti-swing mechanical arms I, II and III, respectively; and φ_x and φ_y are the pitch-swaying angle and roll-swaying angle of the ship, respectively. α is the slewing angle, and β is the luffing angle of the offshore crane. θ_x and θ_y are the swing angles of the payload in the $y_7o_7z_7$ - and $x_7o_7z_7$ -planes. The matrix ${}^3P_M = [{}^3x_M \quad {}^3y_M \quad {}^3z_M]$ is defined the spatial position coordinates of point M in the T_3 coordinate system, where 3x_M , 3y_M and 3z_M represent the x-, y- and z-axis coordinates of point M in the T_3 coordinate system, respectively. A similar method can be used to define the spatial position coordinates of the other points in different coordinate systems.

The swing space of the payload is defined as the area of the real-time trajectory curve formed by the projection of the swinging payload onto the swinging plane in the stable hoisting experiments. The swinging plane of the payload is defined as the centre plane of mass of the payload, and is parallel to the ship-based plane. The drive tension in the anti-swing cables and lifting cable is defined as the tension that drives the swinging motion of the payload, whereas the anti-swing tension is defined as the tension that restrains the swinging motion of the payload. The actual tension in the cables is the sum of the drive and anti-swing tensions. T_3 is invariant, and T_3, T_4, T_5, T_6, T_7 and T_8 are mutative during the coordinate transformation. The relative positions are related to the external excitation of the ship, the mechanical parameters and motion state of the offshore crane. As the coordinate systems are Cartesian, the theory of spatial pose transformation of coordinates is suitable for solving for the position transformation relationship between the different coordinate systems.

The transformation equation for the coordinate points is as follows:

$${}^3P_M = {}^7R {}^7P_M + {}^7S \quad (10)$$

where 7R is the rotation transformation matrix from T_3 to T_7 , and 7S is the translation transformation matrix T_3 to T_7 . The matrices 7R and 7S are calculated as follows:

$${}^7R = {}^3R_x {}^3R_y {}^4R_z {}^6R_x \quad (11)$$

$${}^7S = {}^4S + {}^5S + {}^6S + {}^7S \quad (12)$$

3R_x is the rotation transformation matrix about the x_3 -axis, and the meanings of the other symbols can be obtained by the same method. The equations used to calculate 7R and 7S were given by Crain [25].

The position coordinates of the points E and M in T_7 can be calculated according to the spatial geometry relations in Fig. 4 as

$${}^7P_E = [0 \quad 0 \quad 0] \quad (13)$$

$${}^7P_M = [x_E + H \sin \theta_x \quad y_E + H \cos \theta_x \sin \theta_y \quad z_E - H \cos \theta_x \cos \theta_y] \quad (14)$$

The position coordinates of the points N_1, N_2 and N_3 in T_7 can be calculated with the same method as

$${}^7P_{N_1} = [0 \quad L_I \cos(\delta_1 - \beta) \quad -L_I \sin(\delta_1 - \beta)] \quad (15)$$

$${}^7P_{N_2} = [L_{FE_2} + L_{II} \cos \delta_2 \quad L_{II} \sin \delta_2 - L_{FE} \cos \beta \quad -L_{FE} \sin \beta] \quad (16)$$

$${}^7P_{N_3} = [-L_{FE_3} - L_{III} \cos \delta_3 \quad L_{III} \sin \delta_3 - L_{FE} \cos \beta \quad -L_{FE} \sin \beta] \quad (17)$$

By combining Equations (10) and (13), the position coordinates of point E in T_3 can be obtained as follows:

$${}^3x_E = \begin{pmatrix} ({}^3x_G + L_{FE} \cos \beta \sin \alpha) \cos \varphi_y \\ + ({}^3y_G + L_{FE} \cos \beta \cos \alpha) \sin \varphi_x \sin \varphi_y \\ - ({}^3z_G + L_{GF} + L_{FE} \sin \beta) \cos \varphi_x \sin \varphi_y \end{pmatrix} \quad (18)$$

$${}^3y_E = \begin{pmatrix} ({}^3y_G + L_{FE} \cos \beta \cos \alpha) \cos \varphi_x \\ + ({}^3z_G + L_{GF} + L_{FE} \sin \beta) \sin \varphi_x \end{pmatrix} \quad (19)$$

$$z_E = \begin{pmatrix} ({}^3x_G + L_{FE} \cos \beta \sin \alpha) \sin \varphi_y \\ - ({}^3y_G + L_{FE} \cos \beta \cos \alpha) \sin \varphi_x \cos \varphi_y \\ + ({}^3z_G + L_{GF} + L_{FE} \sin \beta) \cos \varphi_x \cos \varphi_y \end{pmatrix} \quad (20)$$

We assume that the slewing, luffing and lifting speeds are zero for the offshore crane. The acceleration equations at point E can be obtained by calculating the second derivatives of Equations (18) to (20).

$$\ddot{y}_E = \begin{pmatrix} \ddot{\varphi}_x \begin{pmatrix} \cos \varphi_x ({}^3z_G + L_{GF} + L_{FE} \sin \beta) \\ - \sin \varphi_x ({}^3y_G + L_{FE} \cos \beta \cos \alpha) \end{pmatrix} \\ - \dot{\varphi}_x^2 \begin{pmatrix} \cos \varphi_x ({}^3y_G + L_{FE} \cos \beta \cos \alpha) \\ + \sin \varphi_x ({}^3z_G + L_{GF} + L_{FE} \sin \beta) \end{pmatrix} \end{pmatrix} \quad (21)$$

$$\ddot{x}_E = \begin{pmatrix} - ({}^3x_G + L_{FE} \cos \beta \sin \alpha) (\ddot{\varphi}_y \sin \varphi_y + \dot{\varphi}_y^2 \cos \varphi_y) \\ + ({}^3y_G + L_{FE} \cos \beta \cos \alpha) (\ddot{\varphi}_x \cos \varphi_x \sin \varphi_y - \dot{\varphi}_x^2 \sin \varphi_x \sin \varphi_y) \\ + ({}^3y_G + L_{FE} \cos \beta \cos \alpha) (\ddot{\varphi}_y \sin \varphi_x \cos \varphi_y - \dot{\varphi}_y^2 \sin \varphi_x \sin \varphi_y) \\ + ({}^3y_G + L_{FE} \cos \beta \cos \alpha) (2\dot{\varphi}_x \dot{\varphi}_y \cos \varphi_x \cos \varphi_y) \\ + ({}^3z_G + L_{GF} + L_{FE} \sin \beta) (\ddot{\varphi}_x \sin \varphi_x \sin \varphi_y + \dot{\varphi}_x^2 \cos \varphi_x \sin \varphi_y) \\ + ({}^3z_G + L_{GF} + L_{FE} \sin \beta) (\dot{\varphi}_y^2 \cos \varphi_x \sin \varphi_y - \ddot{\varphi}_y \cos \varphi_x \cos \varphi_y) \\ + ({}^3z_G + L_{GF} + L_{FE} \sin \beta) (+2\dot{\varphi}_x \dot{\varphi}_y \sin \varphi_x \cos \varphi_y) \end{pmatrix} \quad (22)$$

$$\ddot{z}_E = \begin{pmatrix} ({}^3x_G + L_{FE} \cos \beta \sin \alpha) (\ddot{\varphi}_y \cos \varphi_y - \dot{\varphi}_y^2 \sin \varphi_x) \\ - ({}^3y_G + L_{FE} \cos \beta \cos \alpha) (\ddot{\varphi}_x \cos \varphi_x \cos \varphi_y - \dot{\varphi}_x^2 \sin \varphi_x \cos \varphi_y) \\ - ({}^3y_G + L_{FE} \cos \beta \cos \alpha) (-\ddot{\varphi}_y \sin \varphi_x \sin \varphi_y - \dot{\varphi}_y^2 \sin \varphi_x \cos \varphi_y) \\ - ({}^3y_G + L_{FE} \cos \beta \cos \alpha) (-2\dot{\varphi}_x \dot{\varphi}_y \cos \varphi_x \sin \varphi_y) \\ - ({}^3z_G + L_{GF} + L_{FE} \sin \beta) (\ddot{\varphi}_x \sin \varphi_x \cos \varphi_y + \dot{\varphi}_x^2 \cos \varphi_x \cos \varphi_y) \\ - ({}^3z_G + L_{GF} + L_{FE} \sin \beta) (-\ddot{\varphi}_y \cos \varphi_x \sin \varphi_y + \dot{\varphi}_y^2 \cos \varphi_x \cos \varphi_y) \\ - ({}^3z_G + L_{GF} + L_{FE} \sin \beta) (-2\dot{\varphi}_x \dot{\varphi}_y \sin \varphi_x \sin \varphi_y) \end{pmatrix} \quad (23)$$

By calculating the second derivative of Equation (14), the acceleration equation for point M can be obtained as follows:

$$\ddot{x}_M = \ddot{x}_E + H [\ddot{\theta}_x \cos \theta_x - \dot{\theta}_x^2 \sin \theta_x] \quad (24)$$

$$\ddot{y}_M = \ddot{y}_E + H \begin{pmatrix} \ddot{\theta}_y \cos \theta_y \cos \theta_x - \dot{\theta}_y^2 \sin \theta_y \cos \theta_x - 2\dot{\theta}_y \dot{\theta}_x \cos \theta_y \sin \theta_x \\ -\ddot{\theta}_x \sin \theta_y \sin \theta_x - \dot{\theta}_x^2 \sin \theta_y \cos \theta_x \end{pmatrix} \quad (25)$$

$$\ddot{z}_M = \ddot{z}_E + H \begin{pmatrix} \ddot{\theta}_y \sin \theta_y \cos \theta_x + \dot{\theta}_y^2 \cos \theta_y \cos \theta_x - 2\dot{\theta}_y \dot{\theta}_x \sin \theta_y \sin \theta_x \\ +\ddot{\theta}_x \cos \theta_y \sin \theta_x + \dot{\theta}_x^2 \cos \theta_y \cos \theta_x \end{pmatrix} \quad (26)$$

When the anti-swing cables are in operation, the length values can be obtained from the geometric relationships shown in Fig. 4, as follows:

$$L_1 = \sqrt{(H \sin \theta_x)^2 + (H \cos \theta_x \sin \theta_y - L_I \cos(\delta - \beta_3))^2 + (H \cos \theta_x \cos \theta_y - L_I \sin(\delta - \beta_3))^2} \quad (27)$$

$$L_2 = \sqrt{(H \sin \theta_x - L_{FE_2} - L_{II} \cos \delta_2)^2 + (H \cos \theta_x \cos \theta_y - L_{FE} \sin \beta)^2 + (H \cos \theta_x \sin \theta_y - L_{II} \sin \delta_2 + L_{FE} \cos \beta)^2} \quad (28)$$

$$L_3 = \sqrt{(H \sin \theta_x + L_{FE_3} + L_{III} \cos \delta_3)^2 + (H \cos \theta_x \cos \theta_y - L_{FE} \sin \beta)^2 + (H \cos \theta_x \sin \theta_y - L_{III} \sin \delta_3 + L_{FE} \cos \beta)^2} \quad (29)$$

By calculating the second derivatives of Equations (27) to (29), the retraction and release speeds of the anti-swing cables can be calculated as follows:

$$\dot{L}_1 = \frac{\begin{pmatrix} H^2 \dot{\theta}_x \sin \theta_x \cos \theta_x + H(H \cos \theta_x \sin \theta_y - L_I \cos(\delta - \beta_3))(\dot{\theta}_y \cos \theta_x \cos \theta_y - \dot{\theta}_x \sin \theta_x \sin \theta_y) \\ -H(H \cos \theta_x \cos \theta_y - L_I \sin(\delta - \beta_3))(\dot{\theta}_x \sin \theta_x \cos \theta_y + \dot{\theta}_y \cos \theta_x \sin \theta_y) \end{pmatrix}}{\sqrt{(H \sin \theta_x)^2 + (H \cos \theta_x \sin \theta_y - L_I \cos(\delta - \beta_3))^2 + (H \cos \theta_x \cos \theta_y - L_I \sin(\delta - \beta_3))^2}} \quad (30)$$

$$\dot{L}_2 = \frac{\begin{pmatrix} H \dot{\theta}_x \cos \theta_x (H \sin \theta_x - L_{FE_2} - L_{II} \cos \delta_2) - H(H \cos \theta_x \cos \theta_y - L_{FE} \sin \beta)(\dot{\theta}_x \sin \theta_x \cos \theta_y + \dot{\theta}_y \cos \theta_x \sin \theta_y) \\ +H(H \cos \theta_x \sin \theta_y - L_{II} \sin \delta_2 + L_{FE} \cos \beta)(\dot{\theta}_y \cos \theta_x \cos \theta_y - \dot{\theta}_x \sin \theta_x \sin \theta_y) \end{pmatrix}}{\sqrt{(H \sin \theta_x - L_{FE_2} - L_{II} \cos \delta_2)^2 + (H \cos \theta_x \cos \theta_y - L_{FE} \sin \beta)^2 + (H \cos \theta_x \sin \theta_y - L_{II} \sin \delta_2 + L_{FE} \cos \beta)^2}} \quad (31)$$

$$\dot{L}_3 = \frac{\begin{pmatrix} H \dot{\theta}_x \cos \theta_x (H \sin \theta_x + L_{FE_3} + L_{III} \cos \delta_3) - H(H \cos \theta_x \cos \theta_y - L_{FE} \sin \beta)(\dot{\theta}_x \sin \theta_x \cos \theta_y + \dot{\theta}_y \cos \theta_x \sin \theta_y) \\ +H(H \cos \theta_x \sin \theta_y - L_{III} \sin \delta_3 + L_{FE} \cos \beta)(\dot{\theta}_y \cos \theta_x \cos \theta_y - \dot{\theta}_x \sin \theta_x \sin \theta_y) \end{pmatrix}}{\sqrt{(H \sin \theta_x + L_{FE_3} + L_{III} \cos \delta_3)^2 + (H \cos \theta_x \cos \theta_y - L_{FE} \sin \beta)^2 + (H \cos \theta_x \sin \theta_y - L_{III} \sin \delta_3 + L_{FE} \cos \beta)^2}} \quad (32)$$

The anti-swing cables are released when the motion speed is positive, and are retracting when the motion speed is negative in Equations (30) to (32).

DYNAMIC MODELING OF AN OFFSHORE CRANE WITH PP-PCDM

A mechanical analysis diagram of the payload is shown in Fig. 3, where \mathbf{F}_{b1} , \mathbf{F}_{b2} and \mathbf{F}_{b3} are the drive tensions of the anti-swing cables I, II, and III, respectively. \mathbf{F}_{b4} is the drive tension of the lifting cable, and \mathbf{F}_5 is the gravitational force on the payload. The flexible nature of the cables is a very important problem that is easy to overlook when analysing the tension in the parallel cables. The cables can only withstand tension, and cannot output thrust; hence, the tension setting of the cables must satisfy unidirectional force conditions, or in other words, the tension in the cables must be positive. The resultant force values in the y_7 -axis direction of \mathbf{F}_{b1} , \mathbf{F}_{b2} , \mathbf{F}_{b3} and \mathbf{F}_{b4} must be less than \mathbf{F}_5 when the direction is opposite to the action of gravity.

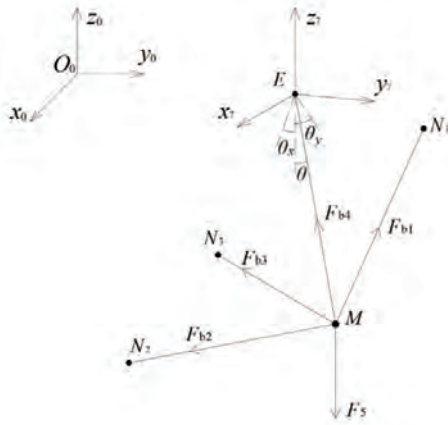


Fig. 5. Mechanical analysis of the payload

The physical relationship satisfies Newton's second law for \mathbf{F}_{b1} , \mathbf{F}_{b2} , \mathbf{F}_{b3} , \mathbf{F}_{b4} and \mathbf{F}_5 , and the tension relationship can therefore be expressed as follows:

$$\mathbf{F}_{b1} + \mathbf{F}_{b2} + \mathbf{F}_{b3} + \mathbf{F}_{b4} - \mathbf{F}_5 = m\mathbf{a} \quad (33)$$

where m is the mass of the payload, and \mathbf{a} is the acceleration of the payload.

From a decomposition of \mathbf{F}_{b1} , \mathbf{F}_{b2} , \mathbf{F}_{b3} and \mathbf{F}_{b4} in the T_7 -axis direction, we obtain:

$$\mathbf{F}_{b1}i_{1x} + \mathbf{F}_{b2}i_{2x} + \mathbf{F}_{b3}i_{3x} + \mathbf{F}_{b4}i_{4x} = m\mathbf{a}_x \quad (34)$$

$$\mathbf{F}_{b1}i_{1y} + \mathbf{F}_{b2}i_{2y} + \mathbf{F}_{b3}i_{3y} + \mathbf{F}_{b4}i_{4y} = m\mathbf{a}_y \quad (35)$$

$$\mathbf{F}_{b1}i_{1z} + \mathbf{F}_{b2}i_{2z} + \mathbf{F}_{b3}i_{3z} + \mathbf{F}_{b4}i_{4z} - \mathbf{F}_5 = m\mathbf{a}_z \quad (36)$$

where i_{1x} , i_{1y} and i_{1z} are the unit vectors in the x_7 -, y_7 - and z_7 -axis directions for anti-swing cable I. The meanings of the other symbols can be obtained via the same method. \mathbf{a}_x , \mathbf{a}_y

and \mathbf{a}_z are the components of the acceleration \mathbf{a} in the axis direction of T_7 .

The unit vectors of the drive tension of the cables in the T_7 direction are calculated as follows:

$$\begin{aligned} i_{1x} &= (x_{N1} - x_M) / L_{MN1} & i_{2x} &= (x_{N2} - x_M) / L_{MN2} & i_{3x} &= (x_{N3} - x_M) / L_{MN3} & i_{4x} &= (x_E - x_M) / L_{ME} \\ i_{1y} &= (y_{N1} - y_M) / L_{MN1} & i_{2y} &= (y_{N2} - y_M) / L_{MN2} & i_{3y} &= (y_{N3} - y_M) / L_{MN3} & i_{4y} &= (y_E - y_M) / L_{ME} \\ i_{1z} &= (z_{N1} - z_M) / L_{MN1} & i_{2z} &= (z_{N2} - z_M) / L_{MN2} & i_{3z} &= (z_{N3} - z_M) / L_{MN3} & i_{4z} &= (z_E - z_M) / L_{ME} \end{aligned}$$

Equations (34) to (36) can be simplified as follows:

$$\mathbf{F}_{bx} + \mathbf{F}_{b4}i_{4x} = m\mathbf{a}_x \quad (37)$$

$$\mathbf{F}_{by} + \mathbf{F}_{b4}i_{4y} = m\mathbf{a}_y \quad (38)$$

$$\mathbf{F}_{bz} + \mathbf{F}_{b4}i_{4z} - \mathbf{F}_5 = m\mathbf{a}_z \quad (39)$$

where \mathbf{F}_{bx} is the combined force of \mathbf{F}_{b1} , \mathbf{F}_{b2} and \mathbf{F}_{b3} in the x_7 -axis direction, and \mathbf{F}_{by} and \mathbf{F}_{bz} have similar meanings.

By substituting Equations (24) to (29) into Equations (37) to (39), the dynamic differential equations for the payload in the x_7 - and y_7 -axis directions can be obtained with appropriate mathematical operations as follows:

$$\ddot{\theta}_x = \frac{\left(\sin \theta_x \left[\sin \theta_y (m\ddot{y}_E - f_{by}) + \cos \theta_y (f_{bz} - mg - m\ddot{z}_E) \right] - \cos \theta_x (f_{bx} - m\ddot{x}_E + mH\dot{\theta}_y^2 \sin \theta_x) \right)}{mH} \quad (40)$$

$$\ddot{\theta}_y = \frac{\left(2H\dot{\theta}_x\dot{\theta}_y \sin \theta_x + \cos \theta_y (f_{by} - m\ddot{y}_E) + \sin \theta_y (f_{bz} - mg - m\ddot{z}_E) \right)}{mH \cos \theta_x} \quad (41)$$

ADAPTIVE TENSION MODELING OF THE PARALLEL CABLES

According to the mathematical relationship in Equations (37) and (38), if the tension in the anti-swing cables I, II and III satisfies the static equilibrium condition in the x_7 - and y_7 -directions, only the tension in the lifting cable acts on the payload in the x_7 - and y_7 -directions. The swinging state of the payload is similar to a pendulum motion subject to air resistance, meaning that the payload is difficult to stabilise quickly. It can be seen from Equations (37) to (39) that the anti-swing cables assist in the hoisting operation of the offshore crane. It is therefore necessary to design an optimisation tension control method that can stabilise the payload from the swinging state quickly.

We therefore propose the ACAT control method, based on the air damping principle, for the self-designed offshore crane with PP-PCDM, in order to restrain the swinging motion of the payload quickly and effectively. First, the swing angle of the payload and the tension in the cables are obtained by high-precision sensors. The spatial position of the payload and the resultant force of the cables are then calculated, and the values of the tension, the swing angle and the spatial

position are used as feedback signals to optimise the tension of the cables. Finally, the length and tension of the anti-swing cables are adjusted in real time, based on the feedback signal, by retracting and releasing operations. The optimised tension of cables consists of the drive tension and the anti-swing tension, where the former is defined in Section 1.4 and the latter is the optimal value for the cable tension. The proposed ACAT control method can rapidly reduce the swing angle and swing space of the payload.

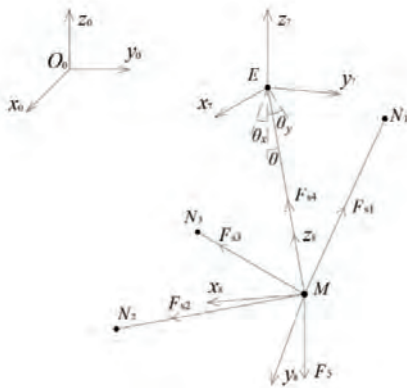


Fig. 6. Mechanical analysis of the payload

A diagram enabling a mechanical analysis of the anti-swing tension is shown in Fig. 6, where F_{s1} , F_{s2} and F_{s3} are the values of the anti-swing tension in anti-swing cables I, II and III, and F_{s4} is the anti-swing tension of the lifting cable. The positive direction of the z_7 -axis is defined as the direction of the centripetal force of the payload, and the force on the x_8y_8 -plane is defined as the centrifugal force of the payload.

The resultant force of F_{s1} , F_{s2} and F_{s3} in the x_7 -axis direction is defined as F_{sx} , and F_{s5} has a similar meaning. F_{sx} and F_{sy} are equivalent to the damping force needed to restrain the swinging motion of the payload in the y_7z_7 -plane and x_7z_7 -plane, respectively. Since the ACAT control method is based on the air damping principle, the formulae used to calculate F_{sx} and F_{sy} are as follows:

$$F_{sx} = k_x F_5 |\dot{\theta}_x| \quad (42)$$

$$F_{sy} = k_y F_5 |\dot{\theta}_y| \quad (43)$$

where k_x and k_y are the anti-swing coefficients in the x_8 -axis and y_8 -axis directions, respectively.

The mathematical relationship between F_{s1} , F_{s2} , F_{s3} , F_{s4} and F_5 is defined as follows:

$$F_s = F_{s1} + F_{s2} + F_{s3} + F_{s4} + F_5 \quad (44)$$

Decomposing the anti-swing tension in the axis direction of T_g , we obtain:

$$F_s s_x = F_{s1} i_{1x} + F_{s2} i_{2x} + F_{s3} i_{3x} + F_{s4} i_{4x} \quad (45)$$

$$F_s s_y = F_{s1} i_{1y} + F_{s2} i_{2y} + F_{s3} i_{3y} + F_{s4} i_{4y} \quad (46)$$

$$F_s s_z = F_{s1} i_{1z} + F_{s2} i_{2z} + F_{s3} i_{3z} + F_{s4} i_{4z} - F_5 \quad (47)$$

Based on the spatial geometry relations in Fig. 4 and Equation (1), the coefficients s_x , s_y and s_z can be calculated as follows:

$$s_x = \frac{-\sin \theta_x \cos \theta_x \cos^2 \theta_y}{\sqrt{(\sin^2 \theta_x \cos^2 \theta_y + \sin^2 \theta_y \cos^2 \theta_x)(1 - \sin^2 \theta_x \sin^2 \theta_y)}} \quad (48)$$

$$s_y = \frac{-\cos^2 \theta_x \sin \theta_y \cos \theta_y}{\sqrt{(\sin^2 \theta_x \cos^2 \theta_y + \sin^2 \theta_y \cos^2 \theta_x)(1 - \sin^2 \theta_x \sin^2 \theta_y)}} \quad (49)$$

$$s_z = \frac{-\sqrt{\sin^2 \theta_x \cos^2 \theta_y + \sin^2 \theta_y \cos^2 \theta_x}}{\sqrt{1 - \sin^2 \theta_x \sin^2 \theta_y}} \quad (50)$$

The controlled parameters are the lengths and tensions of the cables, and the judgment condition is based on the direction of the swing angle and the swing speed of the payload. The detailed rules for the proposed ACAT control method are as follows.

(1) The retracting and releasing operations of the cables are controlled as follows:

$$\begin{cases} \text{if } \theta_x > 0 & \dot{L}_{MN1} < 0 & \dot{L}_{MN2} > 0 & \dot{L}_{MN3} < 0 \\ \text{if } \theta_x < 0 & \dot{L}_{MN1} > 0 & \dot{L}_{MN2} < 0 & \dot{L}_{MN3} > 0 \end{cases}, \begin{cases} \text{if } \theta_y > 0 & \dot{L}_{MN1} > 0 & \dot{L}_{MN2} < 0 & \dot{L}_{MN3} < 0 \\ \text{if } \theta_y < 0 & \dot{L}_{MN1} < 0 & \dot{L}_{MN2} > 0 & \dot{L}_{MN3} > 0 \end{cases} \quad (51)$$

(2) The real values of the tension in the cables are as follows:

$$\begin{cases} \text{if } \dot{\theta}_x > 0 & F_1 = F_{s1} & F_2 = F_{s2} + F_{s2} & F_3 = F_{s3} + F_{s3} \\ \text{if } \dot{\theta}_x < 0 & F_1 = F_{s1} + F_{s1} & F_2 = F_{s2} & F_3 = F_{s3} + F_{s3} \end{cases}, \begin{cases} \text{if } \dot{\theta}_y > 0 & F_1 = F_{s1} + F_{s1} & F_2 = F_{s2} + F_{s2} & F_3 = F_{s3} \\ \text{if } \dot{\theta}_y < 0 & F_1 = F_{s1} + F_{s1} & F_2 = F_{s2} & F_3 = F_{s3} \end{cases} \quad (52)$$

where F_1 , F_2 and F_3 are the real tensions in anti-swing cables I, II and III. The drive tension can be obtained using Equations (33)–(39), the dynamic differential equation for the payload can be obtained from Equations (40) and (41), and the anti-swing tension can be obtained from Equations (42)–(50).

DYNAMIC ANALYSIS OF AN OFFSHORE CRANE WITH PP-PCDM

The design parameters of the experimental ship and the types of signal used for excitation of the ship are two very important parameters for the dynamic model. In order to improve the realism and accuracy of the dynamic ship swaying model, the instructional ship at Dalian Maritime University was used as an experimental platform, and the excitation signal for the ship was stochastic ocean waves. The parameters of the stochastic ocean waves were obtained from Table 1, and the design parameters for the experimental ship are shown in Table 2. A real-time curve for the ship's

swinging motion was obtained by substituting the design parameters of the ship and the parameters of the stochastic ocean waves into Equation (9).

Tab. 2. Design parameters for the instructional ship at Dalian Maritime University

| | | | | | |
|-----------------------------------|---|----------------------|-------------------------|-----------------------------|-----------------|
| Ship length: 109 m | Ship beam: 19 m | Tonnage: 6500 t | Draft: 6 m | Bilge keel length: 21.8 m | Metacentre: 1.5 |
| Bilge keel beam: 0.49 m | Equivalent ship height: 9 m | Eigen period: 12.5 s | Block coefficient: 0.56 | Damping coefficient: 0.1202 | |
| Midship section coefficient: 0.98 | Distance of the swaying axis from the still water surface: 8.28 m | | | | |

In order to verify the correctness of the dynamic model and further improve the authenticity of the simulation experiment, a set of three control simulation experiments were carried out, with conditions as follows: (i) the experimental group, in which the the excitation signal of the ship was stochastic ocean waves; (2) control group 1, in which the excitation signal of the ship was regular ocean waves, and the maximum swaying amplitude and swaying period were the same as for the experimental group; (3) control group 2, where the swinging motion of the ship was regular, and the maximum swaying amplitude and swaying period were the same for the experimental group and control group 1. Graphs of the ship's swaying angle under the three conditions used in the simulation experiments are presented below for comparison.

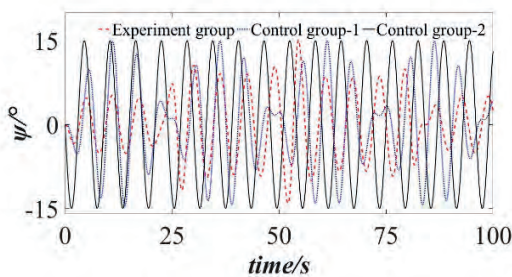


Fig. 7. Sway curves for the ship

As can be seen from Fig. 7, although the real-time curves for the ship's swaying motion are quite different under different ocean conditions, the maximum amplitude and the overall period are the same. The graph for control group 1 is a typical sinusoidal curve, with a regular amplitude and period, whereas the curves for the experimental group show typical irregular characteristics, without a fixed amplitude or period, and the characteristics of control group 2 lie between those of control group 1 and the experimental group, with a relatively stable amplitude and a regular period. Two methods are used to describe and calculate the stabilisation control effect of the offshore crane with PP-PCDM: in the first, we calculate the swing angle based on the swing angle curve of the payload, and in the second, we calculate the swing space based on the trajectory of movement of the payload. The formulae used to compute these are as follows:

$$\eta_{ax} = \frac{\theta_{xb} - \theta_{xa}}{\theta_{xb}} \quad (53)$$

$$\eta_{ay} = \frac{\theta_{yb} - \theta_{ya}}{\theta_{yb}} \quad (54)$$

$$\eta_s = \frac{S_b - S_a}{S_b} \quad (55)$$

where η_{ax} is the stabilisation control effect of the swing angle, θ_{xb} is the maximum value of θ_x for the offshore crane without PP-PCDM, and θ_{xa} is the maximum value of θ_x for the offshore crane with PP-PCDM, as given in Equation (53). The definition in Equation (54) is similar to Equation (53). η_s is the stabilisation control effect of the swing space, S_b is the maximum swing space of the payload for the offshore crane without PP-PCDM, and S_a is the maximum swing space of the payload for the offshore crane with PP-PCDM, as shown in Equation (55). The dynamic simulation analysis of the payload was based on the ship sway model. The parameters of the offshore crane with PP-PCDM were set as follows: $L_{base}=0.42$, $L_{FE2}=L_{FE3}=0.16$, $L_I=0.4$, $L_{II}=0.5$, $L_{III}=0.5$, $L_{FE}=1.2$ m, $\alpha=0^\circ$, $\beta=\pi/3$, $\delta_1=\delta_2=\delta_3=\pi/3$, and $m=20$ kg. The dynamic differential equation for the ship can be obtained from Equation (9), and the dynamic differential equations for the payload from Equation (40) and (41). Figs. 8 to 17 show the results of the digital simulation.

The digital simulation results for the payload swing angle and swing space under the ocean conditions defined for the experimental group are presented below.

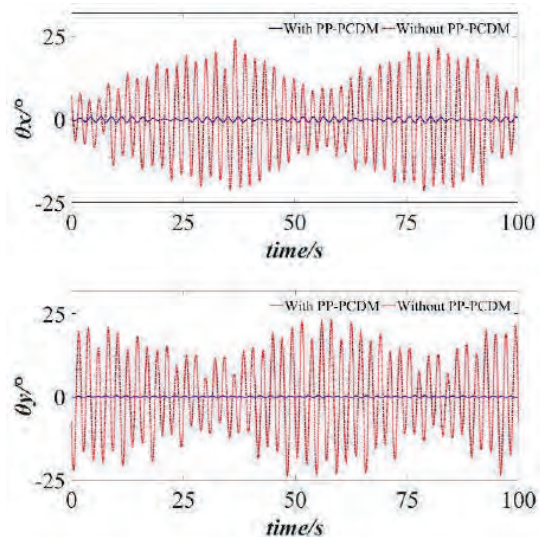


Fig. 8. Swing angle of the payload

As shown in Fig. 8, the values of θ_x and θ_y are not only positive but also negative, indicating the direction of swing of the payload on the x_z -axis and y_z -axis. The payload is in a stable state when $\theta_x = \theta_y = 0$. The values for other angles have the same meaning, and the following part is not repeated.

It can be seen that the angle curve has strong nonlinear and irregular characteristics, and the digital simulation results further prove the practicability of the proposed PP-PCDM. The swing range of θ_x is reduced to $[21.37^\circ, 24.00^\circ]$ for the offshore crane without PP-PCDM. It is clear that θ_x is substantially reduced when PP-PCDM is added, as the swing range becomes $[-0.88^\circ, 0.91^\circ]$. The value of θ_x is reduced from 45.37° ($21.37+24.00$) to 1.79° ($0.88+0.91$), and the reduction in swing can be calculated by Equation (53) as

$$\eta_{ax} = \frac{45.37 - 1.79}{45.37} = 96.05\%$$

The swing ranges of θ_y are $[-23.79^\circ, 23.16^\circ]$ and $[-0.27^\circ, 0.41^\circ]$, and the value of θ_y is reduced from 46.95° to 0.68° with the same method. The swing reduction can be calculated with Equation (54) as

$$\eta_{ay} = \frac{46.95 - 0.68}{46.95} = 98.55\%$$

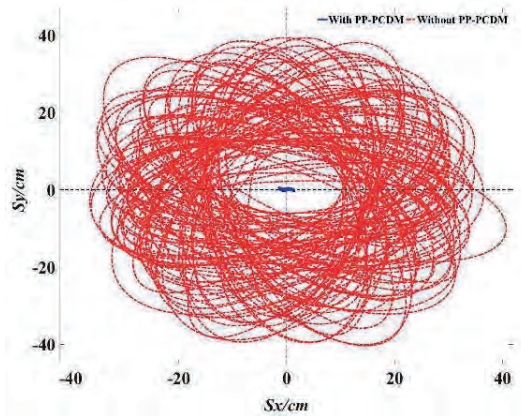


Fig. 9. Swing space of the payload

The motion trajectory of the payload is shown in Fig. 9. The farthest points are 36.61 cm and 40.68 cm in the negative and positive directions of the x_z -axis, respectively, and 40.37 cm and 39.32 cm in the negative and positive directions of the y_z -axis, respectively. The swing space of the payload is calculated as 4836cm^2 in the mathematical simulation for the offshore crane without PP-PCDM. The farthest points are $[1.54\text{ cm}, 1.58\text{ cm}, 0.48\text{ cm}, 0.71\text{ cm}]$ in the four directions, and the swing space is calculated as 1.86cm^2 with the same method. It is obvious that the swing space is significantly reduced when the offshore crane is used with PP-PCDM. The reduction in swing can be calculated using Equation (55) as

$$\eta_s = \frac{4836 - 1.86}{4836} = 99.96\%$$

The digital simulation results for the payload swing angle and swing space under the ocean conditions defined for control group 1 are presented below.

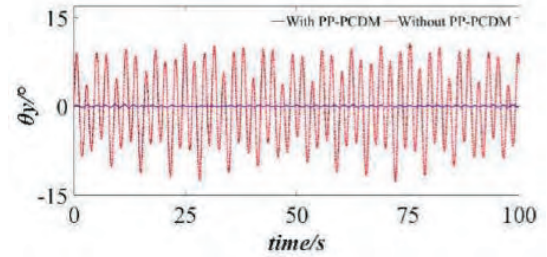
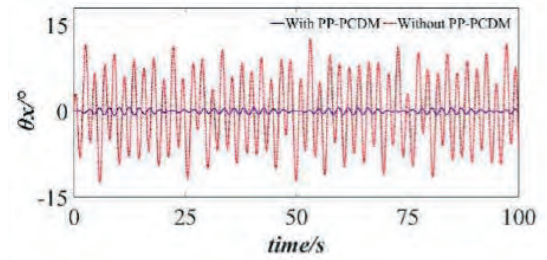


Fig. 10 Swing angle of the payload

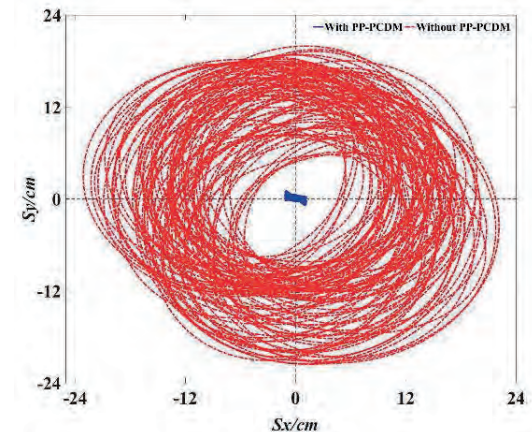


Fig. 11 Swing space of the payload

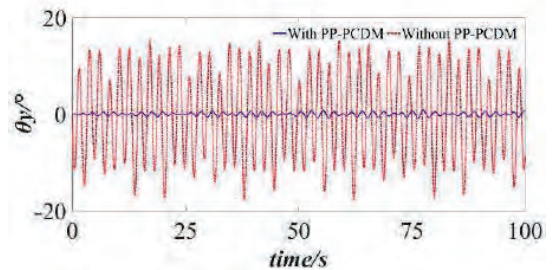
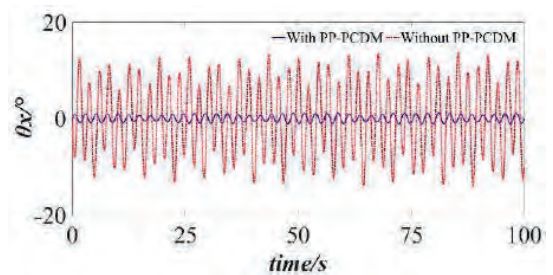


Fig. 12 Swing angle of the payload

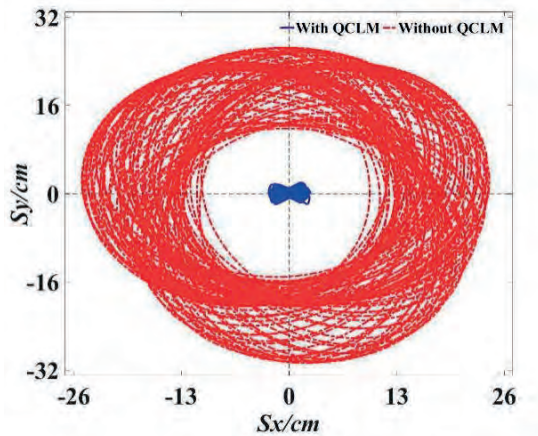


Fig. 13 Swing space of the payload

The simulation results in Figs. 10 and 11 show reduced nonlinear and irregular characteristics relative to Figs. 8 and 9. The variation in the payload's maximum swing angle for different swinging periods is relatively small when the excitation from the ocean waves is regular. The shape of the motion trajectory of payload becomes more regular, i.e. more circular. The swing reduction exceeds 94.65% and 95.37%, as shown in Fig. 10, and the swing space of the payload is reduced by 99.89%, as shown in Fig. 11.

The digital simulation results for the swing angle and swing space of the payload under the ocean conditions of control group 2 are as shown in Figs. 12 and 13. The motion state and trajectory of the payload is similar to that shown in Figs. 8–11.

The simulation results show demonstrate the excellent stabilisation control effect of the swing angle and swing space of the payload under the ocean conditions represented by the experimental group, control group 1 and control group 2. The simulation results are summarised in Table 3.

Tab. 3. Summary of experimental and analytical results

| No. | Experimental results | Swinging angle (without) | Swinging angle (with) | Swing reduction |
|-----|----------------------|--------------------------|-----------------------|-----------------|
| 1 | Fig. 19 | 13.94° | 4.67° | 66.50% - 100% |
| 2 | Fig. 20 | 15.24° | 6.28° | 58.79% - 100% |
| 3 | Fig. 21 | 506.5 | 44.6 | 91.19% - 100% |
| 4 | Fig. 22 | 23.62° | 7.93° | 66.43% - 100% |
| 5 | Fig. 23 | 28.34° | 11.77° | 58.47% - 100% |
| 6 | Fig. 24 | 1583.7 | 141.9 | 91.04% - 100% |

The motion of the anti-swing cables is synchronous with the payload, meaning that a simulation analysis of the lengths and speeds of the anti-swing cables is important. The lengths and speeds of the cables are calculated by Equations (27)–(29) and (30)–(32), respectively. A simulation analysis was conducted based on the ocean conditions of the experimental group, and the results are presented below.

In Fig. 14, the length ranges of anti-swing cables I, II and III are [1.05 m, 1.29 m], [0.37 m, 0.99 m] and [0.38 m, 0.98 m], respectively.

In Fig. 15, V_1 is the retracting and releasing speed of anti-swing cable I, V_2 is the retracting and releasing speed of anti-swing cable II, and V_3 is the retracting and releasing speed of anti-swing cable III. The speed ranges of the three anti-swing cables are $[-0.33 \text{ m/s}, 0.31 \text{ m/s}]$, $[-0.88 \text{ m/s}, 0.86 \text{ m/s}]$ and $[-0.79 \text{ m/s}, 0.78 \text{ m/s}]$, respectively. A negative value for the speed indicates that the anti-swing cables are being retracted, and a positive value means that they are being released. The results of the digital simulation demonstrate the excellent dynamic following performance of the anti-swing cables.

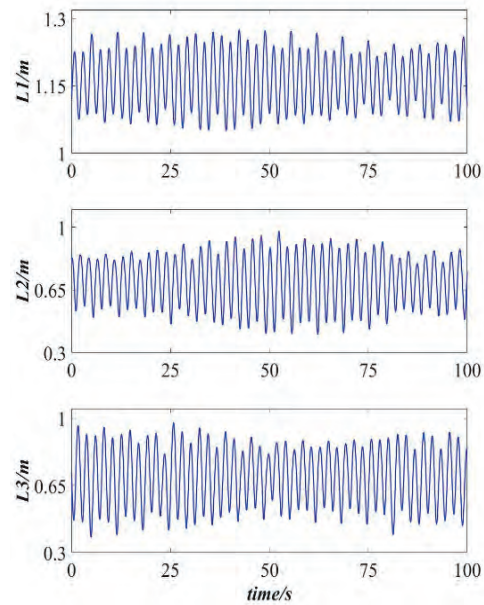


Fig. 14. Length curves for the cables

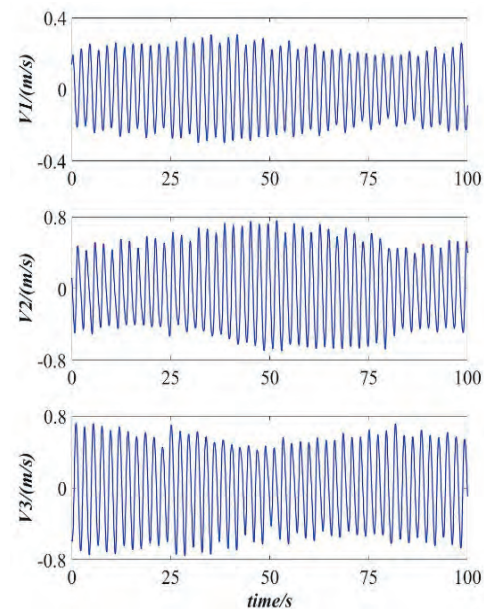


Fig. 15. Speed curves for the cables

A simulation analysis of the relationship between the tension in the lifting cable and the mass of the payload was

carried out based on the mechanical equations in Section 1.4 and the ocean conditions for the experimental group. The results are presented below.

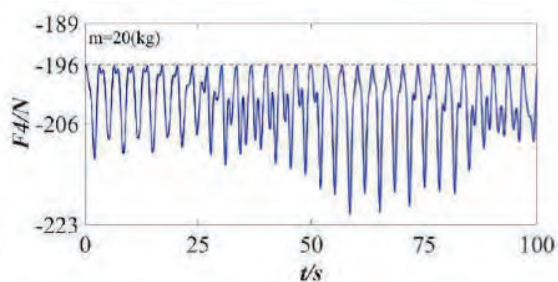


Fig. 16. Tension in the lifting cables

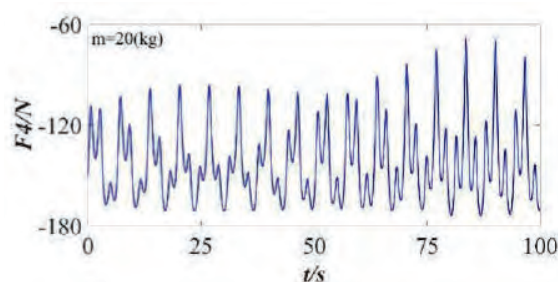


Fig. 17. Tension in the lifting cables

In Fig. 16, negative values indicate that the tension is in the opposite direction to gravity. The tension range of the lifting cable is $[-221.3 \text{ N}, -196.0 \text{ N}]$ when $F_1=F_2=F_3=0$, and it is obvious that the absolute value of the tension in the lifting cable is larger than the gravitational force on the payload. This means that the actual lifting weight will be less than the rated lifting capacity of the offshore crane. Hence, in order to ensure that the rated lifting capacity of the offshore crane is not affected, it is necessary to increase the tension of the anti-swing cables to provide an additional pull on the payload.

As shown in Fig. 17, the tension range of the lifting cable is reduced to $[-174.6 \text{ N}, -67.7 \text{ N}]$ when the tension in the anti-swing cables is increased. The absolute value of the tension in the lifting cable is less than the gravitational force on the payload, meaning that the rated lifting capacity of the offshore crane will not be affected by the swinging motion of the payload. This further demonstrates that the offshore crane with PP-PCDM can not only restrain the swinging amplitude of the payload, but also assist with the hoisting operation.

The following conclusions can be drawn from the results of the digital simulations.

- (1) The proposed PP-PCDM has a strong anti-swing control effect in both the x- and y-directions.
- (2) The swinging state of the payload varies greatly under different excitations from ocean waves. The irregularity in the payload swinging motion becomes more obvious as the payload swing space increases under the strong stochasticity of ocean waves excitation.
- (3) The swing angle only reflects the position of the payload relative to the lifting point, and the swing space is a better

parameter to reflect the position of the payload relative to the deck. The operational safety and efficiency can only be substantially improved when the payload is stationary relative to the deck. The swing space is therefore more beneficial in terms of reflecting the danger from the swinging motion of the payload to the workers on the deck, whereas the swing angle is more useful for building a kinematic and dynamic model of the offshore crane.

EXPERIMENTAL PLATFORM AND EXPERIMENTAL RESEARCH

In order to further verify the effectiveness of the proposed PP-PCDM, an original experimental platform based on a scale model machine was designed and built. The principles and structure were described in Section 1.1, and will not be detailed here. An experiment to explore the swing of the payload was carried out using the experimental platform shown in Fig. 18, in which the cables were controlled with the rules in Equation (51) and the tension was controlled with the rules in Equation (52). The size of the mechanical structure and the system parameters were the same as in the dynamic modelling section. The swaying excitation of the ship was as follows: a swaying angle of 5° with a swaying period of 5 s; and a swaying angle of 10° and a swaying period of 5 s. As the excitation of the ship from ocean waves is not unidirectional in a real marine environment, a compound swaying excitation involving rolling and pitching was used with the platform, in order to improve the authenticity of the experiments. The same method as for the simulation experiments was used to analyse the results.

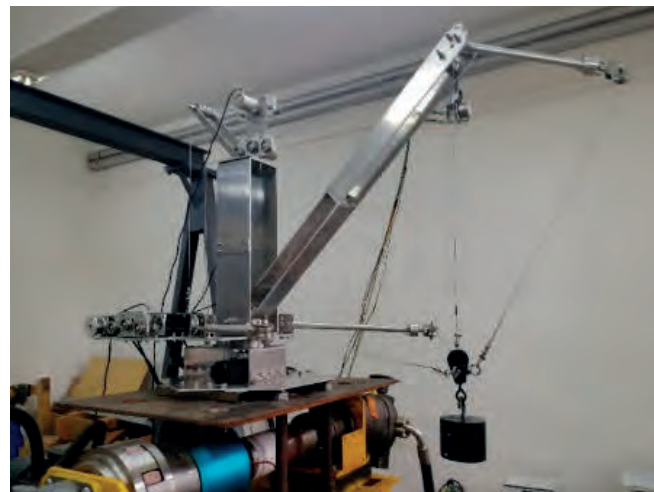


Fig. 18. Photograph of the scale model experimental platform

A summary of the different experimental conditions is shown in Table 4.

Tab. 4 Experimental conditions for the contrast experiments

| No. | Compound swaying excitation | Offshore crane |
|-----|-----------------------------|-----------------|
| 1 | $y=5\sin(2\pi/5)$ | With PP-PCDM |
| 2 | $y=5\sin(2\pi/5)$ | Without PP-PCDM |
| 3 | $y=10\sin(2\pi/5)$ | With PP-PCDM |
| 4 | $y=10\sin(2\pi/5)$ | Without PP-PCDM |

(1) The experimental conditions for the contrast experiment were set to conditions 1 and 2, and the results for the payload swinging amplitude are given below.

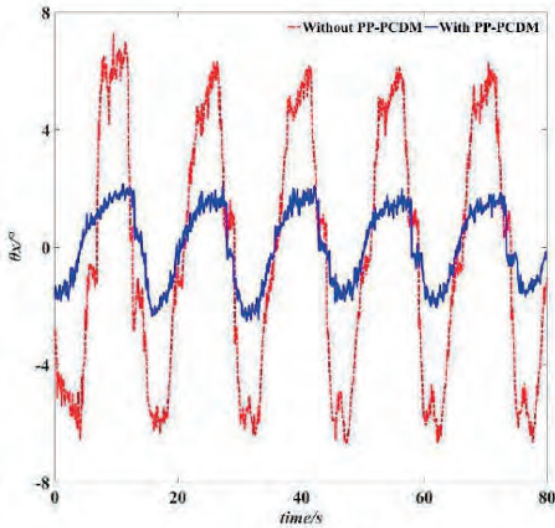


Fig. 19. Swing angle θ_x of the payload

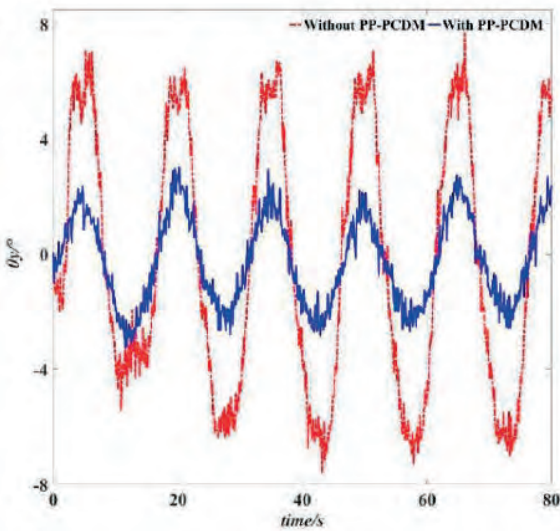


Fig. 20. Swing angle θ_y of the payload

As shown in Fig. 19, the swing range of θ_x is $[-6.67^\circ, 7.27^\circ]$ for the offshore crane without PP-PCDM. However, with the addition of PP-PCDM, θ_x is substantially reduced, and the swing range of θ_x is $[-2.73^\circ, 1.94^\circ]$. The average anti-swing effect is 66.50%, calculated using Equation (53). The minimum and maximum anti-swing effects are 62.45% and 100%, respectively, when calculated with this method. The average anti-swing results indicate the overall effectiveness of the proposed PP-PCDM. The minimum anti-swing effect indicates that θ_x is affected by the resonance between the swinging motion of the payload and the swaying motion of the ship, while the maximum anti-swing effect indicates that the payload can be stabilised to the equilibrium state.

As shown in Fig. 20, the swing range of θ_y is $[-7.56^\circ, 7.68^\circ]$ for the offshore crane without PP-PCDM, whereas the range for θ_y is significantly reduced to $[-3.36^\circ, 2.92^\circ]$ after installing PP-PCDM. The average reduction in swing is 58.47%, and the minimum and maximum reductions in the swing of the payload are found to be 54.18% and 100%, respectively, with this method.

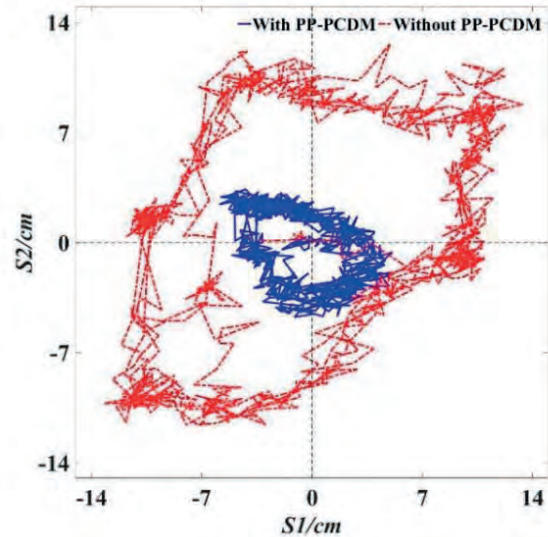


Fig. 21. Swing space of the payload

The swing space method was used to describe the motion state of the payload, and the experimental results for the payload motion trajectory are shown in Fig. 21. The swing space of the payload is in the range $[-13.16 \text{ cm}, 13.36 \text{ cm}, -11.62 \text{ cm}, 12.65 \text{ cm}]$, and the swing space of the payload is 506.5 cm^2 for the offshore crane without the PP-PCDM. However, with the addition of the PP-PCDM, the swing space is markedly reduced to the range $[-5.86 \text{ cm}, 5.10 \text{ cm}, -3.38 \text{ cm}, 4.76 \text{ cm}]$ and the swing space of the payload is 44.6 cm^2 . The reduction in swing is 91.19% when calculated with the same method. The swing space of the payload is limited to only 8.81% of the original swing space without PP-PCDM.

(2) The experimental conditions for the contrast experiment were set to conditions 3 and 4, and the results for the payload swinging amplitude comparison are given below.

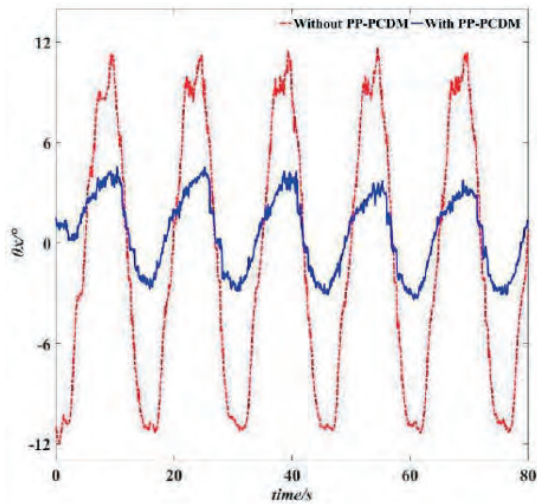


Fig. 22. Swing angle θ_x of the payload

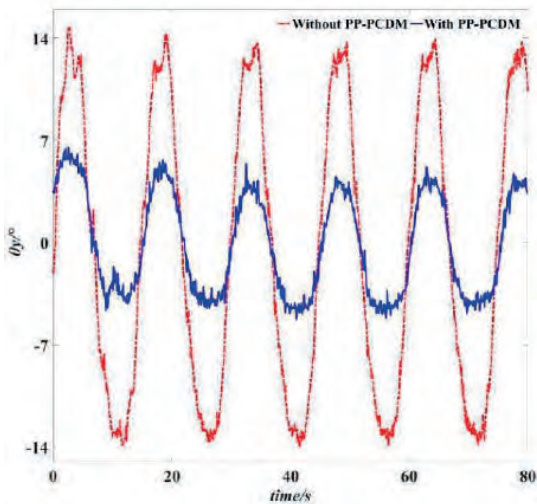


Fig. 23. Swing angle θ_y of the payload

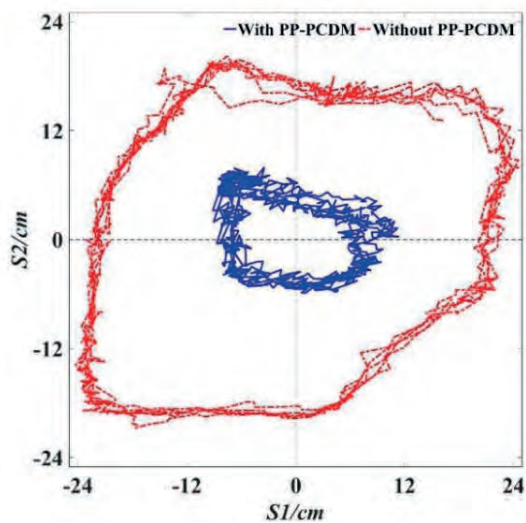


Fig. 24. Swing space of the payload

From Figs. 22–24, we see that the motion state and trajectory of the payload and the reduction in swing are similar to those shown in Figs. 19–21; however, the swing angle and swing space of the payload rise significantly when the amplitude of the ship’s swaying excitation is increased. The experimental results are summarised in Table 5.

Tab. 5 Summary of experimental and analytical results

| No. | Experimental results | Swinging angle (without) | Swinging angle (with) | Swing reduction |
|-----|----------------------|--------------------------|-----------------------|-----------------|
| 1 | Fig. 19 | 13.94° | 4.67° | 66.50% - 100% |
| 2 | Fig. 20 | 15.24° | 6.28° | 58.79% - 100% |
| 3 | Fig. 21 | 506.5 | 44.6 | 91.19% - 100% |
| 4 | Fig. 22 | 23.62° | 7.93° | 66.43% - 100% |
| 5 | Fig. 23 | 28.34° | 11.77° | 58.47% - 100% |
| 6 | Fig. 24 | 1583.7 | 141.9 | 91.04% - 100% |

The results of the physical experiments are similar to those of the digital simulations. The feasibility and correctness of the dynamic model is demonstrated, and the effectiveness and practicability of the designed PP-PCDM is proved. The robustness of the proposed ACTC control method is also verified for an offshore crane working under different ocean conditions.

A comparison of the results in Tables 3 and 5 shows that the swing angle and swing space of the payload in the three-dimensional space is drastically reduced following addition of the PP-PCDM. The safety of the workers on deck is significantly improved, and the efficiency of the hoisting operation of the offshore crane is also markedly improved.

By comparing the maximum values of θ_x and θ_y in the same digital simulation or physical experiment, we see that θ_y is slightly larger than θ_x . The reason for this difference can be obtained by analysing the experimental results and the dynamic model of the offshore crane. The central axis of the ship’s transverse swaying motion is located in the $y_7o_7z_7$ -plane, whereas the central axis of the ship’s longitudinal swaying motion is not located in this plane. This is equivalent to adding an eccentric motion to the payload in the $y_7o_7z_7$ -plane, and means that the maximum value of θ_y is slightly larger than for θ_x .

A comparison of the swinging amplitude of payload for offshore cranes working under different ocean conditions indicates that the swinging amplitude of the payload will gradually increase when the swaying excitation amplitude of the ship is increased. In other words, the more complex the ocean conditions, the larger the swinging amplitude of the payload.

In order to further test the stability and robustness of the PP-PCDM under external disturbance such as ocean winds or vibration, a physical experiment was set up to reflect real ocean conditions. An external interference experiment was carried out, and the experimental results are given below.

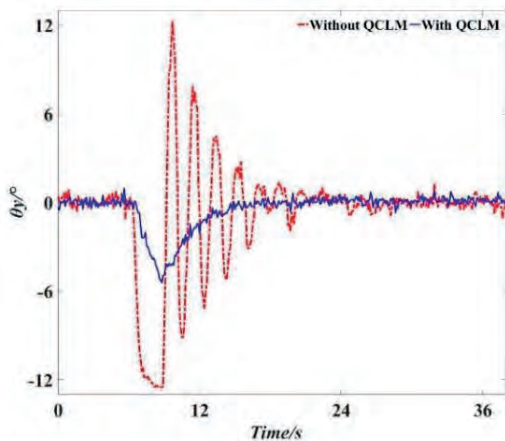


Fig. 25. Swing angle of the payload under external disturbance

As shown in Fig. (25), the payload is in a stable state for the first 6 s, and the swing range of θ_y is $[-0.57^\circ, 0.88^\circ]$ for an offshore crane without PP-PCDM. However, with the addition of the PP-PCDM, the swing-range of θ_y is $[-0.50^\circ, 0.51^\circ]$. It can be seen that the synchronous motion of the cables following the payload can also limit the spatial position of the payload, even if the ACAT control method is not applied to the cables. A disturbing force is applied to the payload in the y_z -axis direction after 6 s. First, θ_y increases rapidly to 12.61° , and then increases to 12.49° in the opposite direction. Finally, the payload reaches a stable state again until 28 s, after repeatedly swinging for multiple periods. Even if the payload reaches the stable state again at 28 s, the swing angle is still larger than the angle of the payload with PP-PCDM in the subsequent time.

The maximum swinging amplitude of the payload is 25° , and this amplitude is reduced after multiple periods for the offshore crane without PP-PCDM. However, it is obvious that the curve for θ_y is completely different when PP-PCDM is applied. The value of θ_y increases and then decreases gradually, and the swing range of θ_y is $[-5.45^\circ, 1.00^\circ]$. The maximum value of θ_y is reduced by 74.2%. The payload returns to a stable state after only half of one swinging period after 15 s, and the swinging speed of the payload is significantly reduced compared to the offshore crane without PP-PCDM. The lower swinging speed of the payload can not only reduce the power requirements of the drive unit, but can also greatly improve the safety of the offshore crane operation. These results indicate that the ATAC control method begins to work immediately when the disturbance force is applied. Hence, the stability and robustness of our PP-PCDM with ACAT control method is demonstrated when the payload is disturbed by external forces.

The results of these dynamic simulations and physical experiments show that the offshore crane with PP-PCDM can accomplish the hoisting operations safely and efficiently in an actual ocean environment, and even under heavy ocean conditions. The proposed PP-PCDM with ACTC control method can not only reduce the swing space of the payload,

but also assist the hoisting operation of the offshore crane. The rated lifting capacity of the offshore crane is not affected by the swinging motion of the payload.

CONCLUSION

An offshore crane with PP-PCDM and ACAT control method has been proposed to solve the problem of swinging of the payload when an offshore crane is working under stochastic ocean wave excitation. A precise dynamic model of the payload and cables was established, and the dynamic characteristics were analysed. The main findings are as follows:

(1) The swinging state of the payload varies greatly under different types of ocean wave excitation. The simulation results indicate that the reduction in the swing angle exceeds 89.86%, the corresponding swing space of the payload is limited, and the swing reduction exceeds 99.56% when the movement and dynamic tension of the parallel cables are controlled.

(2) Physical experiments further proved the correctness of our dynamic model and the results of the simulation analysis under compound swinging excitation of the ship. The swing space and swing angle of the payload gradually increase when the amplitude of swaying excitation of the ship is increased. The experimental results show that the reduction in the swing space exceeds 91.04% and 91.19%.

(3) The proposed control method based on PP-PCDM with ACAT shows excellent stability and robustness under different ocean conditions, and ensures that the rated lifting capacity of the offshore crane is not affected. The operational safety of an offshore crane is improved considerably, meaning that it can work efficiently under complicated ocean conditions.

ACKNOWLEDGEMENTS

This work was financially supported by the National Natural Science Foundation of China (Project No. 52101396), the National Key Research and Development Program of China (Project No. 2022YFB4300802), and China Fundamental Research Funds for the Central Universities (Project No. 3132023510).

DISCLOSURE STATEMENT

No possible conflicts of interest were identified by the authors.

REFERENCES

1. Hongzhang J, Xuliang Y. Ship control principle, second edition. Harbin Engineering University Press; 2001.
2. Li Z, Ma X, Li Y. Anti-swing control for a double-pendulum offshore boom crane with ship roll and heave movements.

- IEEE 16th International Conference on Control and Automation, pp. 165-170, Oct. 2020. DOI:10.1109/ICCA51439.2020.9264524.
3. Konrad Johan J, Ebbesen M, Hansen M. Development of point-to-point path control in actuator space for hydraulic knuckle boom crane. *Modeling, Identification and Control*, vol. 42, no. 3, pp. 113-129, 2021. DOI: 10.3390/act9020027.
 4. Shamseldin M. Design of auto-tuning nonlinear PID tracking speed control for electric vehicle with uncertainty consideration. *World Electric Vehicle Journal*, vol. 14, no. 4, Apr. 2023. DOI: 10.3390/wevj14040078.
 5. De Kruif B, Rossin B. Pendulation control for dynamical positioning capable ship; Considerations on actuator usage. *IFAC Papers Online*, vol. 54, no. 16, pp. 120-125, Nov. 2021. DOI: 10.1016/j.ifacol.2021.10.082.
 6. Goodarzi R, Korayem M, Tourajizadeh H, et al. Nonlinear dynamic modeling of a mobile spatial cable-driven robot with flexible cables. *Nonlinear Dynamics*, vol. 108, no. 4, pp. 3219-3245, Jun. 2022. DOI: 10.1007/s11071-022-07397-4.
 7. Ashkoofaraz S, Lori A. Aerial load transportation with obstacle avoidance in observed environment. 2022 10th RSI International Conference on Robotics and Mechatronics, pp. 248-253. 2022. DOI: 10.1109/ICRoM57054.2022.10025232.
 8. Casas J, Chang C, Duenas V. Switched adaptive concurrent learning control using a stance foot model for gait rehabilitation using a hybrid exoskeleton. *IFAC Papers Online*, vol. 55, no. 41, pp. 187-192, Feb. 2023. DOI:10.1016/j.ifacol.2023.01.124.
 9. Shenghao T, Huaitao S, Peng Z, et al.. Research on accurate motion control of cable crane based on variable structure sliding mode. *Journal of the Brazilian Society of Mechanical Sciences and Engineering*, vol. 45, no. 6, p. 316, Jun. 2023. DOI:10.1007/s40430-023-04236-4.
 10. Bin G, Yong C. Fuzzy robust fault-tolerant control for offshore ship-mounted crane system. *Information Sciences*, vol. 526, pp. 119-132, Jul. 2020. DOI: 10.1016/j.ins.2020.03.068.
 11. Manh Cuonga H, Van Thai N, et al. Nonsingular fractional-order integral fast-terminal sliding mode control for under actuated shipboard cranes. *Journal of the Franklin Institute*, vol. 359, pp. 6587-6606, 2022. DOI: 10.1109/CDC.2014.7040128.
 12. Lu B, Fang Y, Sun N, et al. Nonlinear coordination control of offshore boom cranes with bounded control inputs. *International Journal of Robust & Nonlinear Control*, vol. 29, no. 4, pp. 1165-1181, Mar. 2019. DOI: 10.1109/ACC.2012.6314810.
 13. Yuzhe Q, Yongchun F, Tong Y. An energy-based nonlinear coupling control for offshore ship-mounted cranes. *International Journal of Automation & Computing*, vol. 15, no. 5, pp. 570-581, Oct. 2018. DOI: 10.1109/TSMC.2017.2700393.
 14. Li X, Peng X, Geng Z. Anti-swing control for 2-D under-actuated cranes with load hoisting/lowering: A coupling-based approach. *ISA Transactions*, vol. 95, pp. 372-378, Dec. 2019. DOI: 10.1016/j.isatra.2019.04.033.
 15. Yuchi C, Tieshan L. Review of anti-swing control of shipboard cranes. *IEEECAA Journal of Automatica Sinica*, vol. 7, no. 2, pp. 346-354, Mar. 2020. DOI: 10.1109/JAS.2020.1003024.
 16. Jianli W, Kexin L, Shenghai W, et al. Dynamic analysis and experiment of underactuated double-pendulum anti-swing device for ship-mounted jib cranes. *Polish Maritime Research*, vol. 29, no. 4, pp. 145-154, Dec. 2022. DOI: 10.2478/pomr-2022-0052.
 17. Shi H, Yao F, Yuan Z, et al. Enhanced-coupling-based tracking control of double pendulum gantry cranes. *International Journal of Control Automation and Systems*, vol. 20, no. 7, pp. 2260-2272, Jul. 2022. DOI: 10.1007/s12555-021-0401-9.
 18. McKenzie R, Irani R. Motion compensation for maritime cranes during time-varying operations at the pendulum's natural frequency. *Mechanism and Machine Theory*, vol. 168, p. 104573, Feb. 2022. DOI: 10.1016/j.mechmachtheory.2021.104573.
 19. Xiyang H, Huanbin L, et al. Application of four-rope theory to integral hoisting of marine booster station. *Engineering Journal of Wuhan University*, vol. 51 (Sup), pp. 304-307, Aug. 2018. DOI: 10.1007/s12206-020-0415-x.
 20. Bozkurt B, Erdogan M. Heave and horizontal displacement and anti-sway control of payload during ship-to-ship load transfer with an offshore crane on very rough sea conditions. *Ocean Engineering*, vol. 267, p. 113309, Jan. 2023. DOI: 10.1016/j.oceaneng.2022.113309.
 21. Menghua Z, Yibin X, Xincheng T. Adaptive tracking control for double-pendulum overhead cranes subject to tracking error limitation, parametric uncertainties and external disturbances. *Mechanical Systems and Signal Processing*, vol. 76, pp. 15-32, Aug. 2016. DOI: 10.1016/j.ymsp.2016.02.013.
 22. Ren Z, Verma A, Ataei B, et al. Model-free anti-swing control of complex-shaped payload with offshore floating cranes and a large number of lift wires. *Ocean Engineering*, vol. 228, p. 108868, May 2021. DOI: 10.1016/j.oceaneng.2021.108868.

23. Casas J, Chang C, Duenas V. Concurrent learning control for treadmill walking using a cable-driven exoskeleton with FES. in American Control Conference, pp. 3019-3024, 2022. DOI: 10.23919/ACC53348.2022.9867186.
24. Ryszard B, Bartłomiej Z. Finite element fatigue analysis of unsupported crane. Polish Maritime Research, vol. 28, no. 1, pp. 127-135, Mar. 2021. DOI:10.2478/pomr-2021-0012.
25. Craig J. Introduction to robotics, mechanics and control, fourth edition. China Machine; 2019.